Astronomy & Astrophysics manuscript no. output
October 14, 2024

Letter to the Editor

Imaging the innermost circumstellar environment of the red supergiant WOH G64 in the Large Magellanic Cloud ⋆

K. Ohnaka[1], K.-H. Hofmann[2], G. Weigelt[2], J. Th. van Loon[3], D. Schertl[2], and S. R. Goldman[4]

[1] Instituto de Astrofísica, Departamento de Ciencias Físicas, Facultad de Ciencias Exactas, Universidad Andrés Bello, Fernández Concha 700, Las Condes, Santiago, Chile
e-mail: `k1.ohnaka@gmail.com`
[2] Max-Planck-Institut für Radioastronomie, Auf dem Hügel 69, 53121 Bonn, Germany
[3] Lennard-Jones School of Chemical and Physical Sciences, Keele University, Staffordshire ST5 5BG, U.K.
[4] Space Telescope Science Institute, 3700 San Martin Drive, Baltimore, MD 21218, U.S.A.

Received / Accepted

ABSTRACT

Context. Significant mass loss in the red supergiant (RSG) phase has great influence on the evolution of massive stars and their final fate as supernovae.

Aims. We present near-infrared interferometric imaging of the circumstellar environment of the dust-enshrouded RSG WOH G64 in the Large Magellanic Cloud.

Methods. WOH G64 was observed with the GRAVITY instrument at ESO's Very Large Telescope Interferometer (VLTI) at 2.0–2.45 μm. We succeeded in imaging the innermost circumstellar environment of WOH G64 – the first interferometric imaging of an RSG outside the Milky Way.

Results. The reconstructed image reveals elongated compact emission with a semimajor and semiminor axis of ~2 and ~1.5 mas (~13 and 9 $R_\star$), respectively. The GRAVITY data show that the stellar flux contribution at 2.2 μm at the time of our observations in 2020 is much lower than predicted by the optically and geometrically thick dust torus model based on the VLTI/MIDI data taken in 2005 and 2007. We found a significant change in the near-infrared spectrum of WOH G64: while the (spectro)photometric data taken at 1–2.5 μm before 2003 show the spectrum of the central RSG with H_2O absorption, the spectra and *JHK′* photometric data taken after 2016 are characterized by a monotonically rising continuum with very weak signatures of H_2O. This spectral change likely took place between December 2009 and 2016. On the other hand, the mid-infrared spectrum obtained in 2022 with VLT/VISIR agrees well with the spectra obtained before 2007.

Conclusions. The compact emission imaged with GRAVITY and the near-infrared spectral change suggest the formation of hot new dust close to the star, which gives rise to the monotonically rising near-infrared continuum and the high obscuration of the central star. The elongation of the emission may be due to the presence of a bipolar outflow or effects of an unseen companion.

Key words. infrared: stars – techniques: interferometric – stars: imaging – (stars:) supergiants – (stars:) circumstellar matter – stars: individual: WOH G64

1. Introduction

Significant mass loss in the red supergiant (RSG) phase is of great importance for the evolution of massive stars before they end their life in a supernova (SN) explosion. The RSGs at advanced evolutionary stages experience drastic mass loss with a mass-loss rate as high as ~10^{-4} $M_\odot$ yr^{-1} (Goldman et al. 2017). Recent analyses of very early-phase spectra of SNe – taken within a day after the explosion – suggest significant increases in the mass-loss rate in the RSG phase before the SN explosion (e.g., Yaron et al. 2017; Moriya et al. 2018; Zhang et al. 2023).

High-spatial-resolution observations of some RSGs reveal salient deviations from spherical symmetry in their circumstellar environment (e.g., Wittkowski et al. 1998; Monnier et al. 2004; Humphreys et al. 2007; O'Gorman et al. 2015). Nonspherical mass loss can also be exemplarily seen in the dust ring around SN1987A, which is considered to have been shed in the RSG phase before the progenitor evolved into a blue supergiant and exploded (Crotts & Heathcoat 1991). Given the high multiplicity rate among massive stars (Mason et al. 2009; Sana et al. 2012), the asymmetric, enhanced mass loss in the RSG phase, which can be driven by binary interaction (e.g., Ercolino et al. 2024; Landri & Pejcha 2024), is essential not only for better understanding the evolution of massive stars but also for interpreting early-phase SN spectra.

The RSGs in the Large Magellanic Cloud (LMC) have the great advantage that their distances are much better known (50 kpc, Pietrzyński et al. 2013) compared to those of their Galactic counterparts. WOH G64 is the brightest RSG in the mid-infrared in the LMC, exhibiting a huge infrared excess with a high mass-loss rate on the order of 10^{-4} $M_\odot$ yr^{-1} (Goldman et al. 2017). For this reason, it has been a subject of multiwavelength studies from the visible to the radio (e.g., van Loon et al. 1996; Levesque et al. 2009; Matsuura et al. 2016). Ohnaka et al. (2008) succeeded in spatially resolving the circumstellar dust environment of WOH

Send offprint requests to: K. Ohnaka

⋆ Based on observations collected at the European Southern Observatory under ESO programmes 106.219D.001, 106.219D.002, 110.23RT.004, 097.D-0605(A), and 71.B-0558(A) as well as at the Rapid Eye Mount Telescope under the Chilean National Time Allocation Committee programme CN2024A-73.

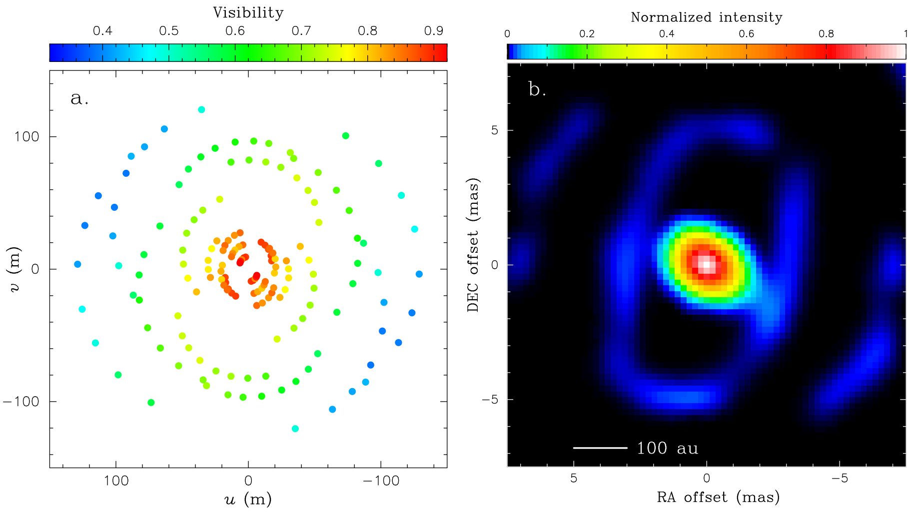

Fig. 1. Visibility and image of WOH G64 obtained from our VLTI/GRAVITY observations. **a:** *uv* coverage of our VLTI/GRAVITY observations of WOH G64 with the calibrated visibility color-coded. North is up, east is to the left. **b:** Image of WOH G64 reconstructed at 2.2 μm (with a spectral window of 0.2 μm) using IRBis with the maximum entropy regularization. North is up, east is to the left.

G64 using the mid-infrared interferometric instrument MIDI at the Very Large Telescope Interferometer (VLTI). Their 2D radiative transfer modeling shows that the observed spectral energy distribution and the visibilities measured at 8–13 μm can be simultaneously reproduced by a geometrically and optically thick torus viewed nearly pole-on. Moreover, the luminosity of $\sim 2.8 \times 10^5$ $L_\odot$ derived from the dust torus model brought WOH G64 to fair agreement with the evolutionary track with an initial mass of 25 $M_\odot$.

However, because MIDI was a two-telescope interferometer, it was not possible to obtain an image of WOH G64. In this Letter, we present the first infrared interferometric imaging of WOH G64.

2. Observations and data reduction

We carried out interferometric observations of WOH G64 with GRAVITY (GRAVITY Collaboration 2017) at VLTI on December 15 and 26, 2020 (UTC), at 2.0–2.45 μm, using the Auxiliary Telescope (AT) configurations A0-G1-J2-J3 and A0-B2-C1-D0 with a maximum projected baseline length of 129 m (Program ID: 106.219D.001/002, P.I.: K. Ohnaka). We also observed HD32956 (F0/2IV/V, uniform-disk diameter = 0.17 mas, JMMC catalog: Bourges et al. 2017) and HD37379 (F6/7V, uniform-disk diameter = 0.16 mas) for the interferometric and spectroscopic calibration. Our GRAVITY observations are summarized in Table A.1.

To increase the signal-to-noise (S/N) of the results, the raw GRAVITY data taken with a spectral resolution of 500 were first spectrally binned using a running box car filter, which resulted in a spectral resolution of 330. The spectral binning was applied to both the science target and the calibrators as well as the raw calibration files needed to create the P2VM. The spectrally binned raw data were then reduced with the GRAVITY pipeline ver 1.4.1[1]. The errors in the calibrated visibilities of WOH G64 were computed from the errors given by the pipeline and the variations in the transfer function calculated from all the calibrators observed on each night.

Figure 1a shows the *uv* coverage of our GRAVITY observations of WOH G64 with the visibility color-coded. The visibility falls off more rapidly in the northeast-southwest direction than in the northwest-southeast direction, which suggests that the object appears larger in the northeast-southwest direction. As Figs. B.1 and B.2 show, the visibilities and closure phases show no trace of the CO bands, although the 2.3 μm band head is weakly seen in the spectrum (Fig. 3b). We reconstructed images from the GRAVITY data using IRBis (Hofmann et al. 2014) and MiRA (Thiébaut 2008). IRBis selects the best reconstruction based on the fit to the measurements and the distribution of the positive and negative residuals between the measured quantities (visibilities and closure phases) and those of the reconstructed image. The best reconstruction with IRBis was obtained with the maximum entropy regularization using the cost functions 1 and 2 defined in Hofmann et al. (2014). For the reconstruction with MiRA, two different regularizations (pixel difference quadratic and pixel intensity quadratic) were employed, and the optimal value of the hyperparameter was determined with the L-curve method. The spectrum of WOH G64 extracted from the GRAVITY data was spectroscopically calibrated, as is described in Appendix C.

We also obtained J-, H-, and K'-band photometric data on August 11, 2024, with the REMIR camera at the Rapid Eye Mount (REM) Telescope[2] (Molinari 2019). Details of the REM observations are described in Appendix D.

3. Results

Figure 1b shows the image reconstructed at 2.2 μm with IRBis using the data between 2.1 and 2.3 μm. The resolution of the image is ~1 mas. Figure E.1 shows comparisons of the measured visibilities and closure phases with those computed from the IRBis reconstructed image. The image reconstructed with MiRA is shown in Fig. E.2, in which only the image obtained with the pixel difference quadratic regularization is presented, because the result obtained with the pixel intensity quadratic regularization is similar.

Both images obtained with IRBis and MiRA reveal compact elongated emission with a major and minor axis of ~4 mas and 3 mas, respectively, with a position angle of the major axis of ~56°. This corresponds to the position angle dependence of the visibility seen in Fig. 1a. The stellar radius of 1730 $R_\odot$ derived by Ohnaka et al. (2008) and the distance of 50 kpc translate into a stellar angular radius of 0.16 mas. Therefore, the semimajor and semiminor axes of the elongated emission correspond to ~13 and ~9 $R_\star$, respectively. The central star does not clearly appear as a point source in our reconstructed image. This could be because

[1] https://www.eso.org/sci/software/pipelines/gravity/

[2] http://www.rem.inaf.it

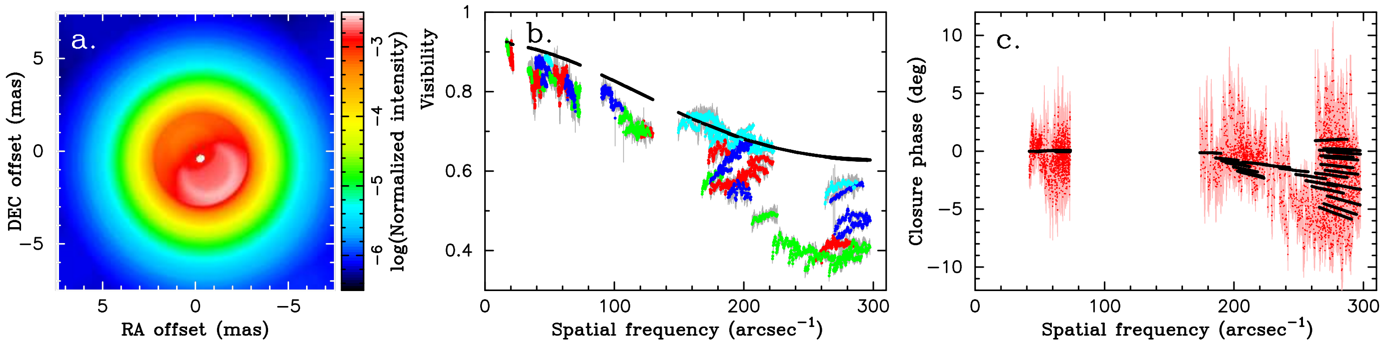

Fig. 2. Comparison of the dust torus model of Ohnaka et al. (2008) with the GRAVITY data. **a:** Image predicted by the dust torus model at 2.2 μm with an inclination angle of 20°. Note that the central star's intensity (white dot at the center) is at least ~400 times higher than that of the torus. North is up, east is to the left. **b:** Comparison of the visibility between the dust torus model and the GRAVITY data. The black dots (they appear to be solid lines due to the high density) represent the 2.2 μm visibilities predicted by the dust torus model. The dots with the error bars represent the GRAVITY data with the position angle (PA) of the projected baseline color-coded: red (0°≤PA<45°), green (45°≤PA<90°), blue (90°≤PA<135°), and light blue (135°≤PA<180°). **c:** Comparison of the closure phase between the dust torus model and the GRAVITY data. The model closure phases are shown in black, while the measurements are plotted with the red dots with the error bars.

the central star is very faint or because it is entirely obscured. The visibilities measured at the longest baselines tend to be flat as a function of spatial frequency (Figs. 2b and E.1a), which can be explained by the presence of a point source. However, data at even longer baselines are needed to confirm this and derive the fractional flux contribution of the central star in the *K* band.

A faint elliptical ring-like structure (≲3% of the peak intensity) with a semimajor and semiminor axis of ~5 mas and 3 mas (~31 and 19 $R_\star$), respectively, can be seen in dark blue in both images reconstructed with IRBis and MiRA. This ring-like structure might be interpreted as the inner rim of a dust disk or torus viewed from an intermediate inclination angle, higher than in the torus model of Ohnaka et al. (2008). The ring's appearance in the images reconstructed with different algorithms (MiRA and IRBis) lends support to it being real. However, as Fig. E.2 shows, the location of the ring is just inside the side lobe of the dirty beam, and therefore we cannot entirely exclude the possibility that it might be an artifact of the image reconstruction inherent in the imperfect *uv* coverage. We refrain from further discussing this structure until we can confirm it with better *uv* coverage.

Figure 2a shows the image predicted at 2.2 μm from the dust torus model of Ohnaka et al. (2008). The model image is characterized by the central star and the emission from the inner rim on the far side (light red to white region in the southwest). To examine whether the model is consistent with the GRAVITY data, we show comparisons of the visibility and closure phase in Figs. 2b and 2c. While the model closure phase is in fair agreement with the measurements, the model predicts the 2.2 μm visibility to be too high compared to the data. We computed 2.2 μm images at different inclination angles within its uncertainty (0–30°) and different position angles in the plane of the sky, but they all show too high visibilities and too little elongation compared to the data. This is because the model predicts the stellar flux contribution at 2.2 μm to be too high compared to the GRAVITY data (note that the central star's intensity is higher than the intensity of the light red to white region in the southwest by a factor of at least ~400).

4. Change in the spectral shape in the infrared

We found evidence that the difference in the 2.2 μm stellar flux contribution could be due to a systematic change in the circumstellar environment of WOH G64 between the MIDI observations in 2005 and 2007 and our GRAVITY observations in 2020. Figure 3a shows (spectro)photometric data of WOH G64 taken before 2010 collected from the literature (Wood et al. 1992; Whitelock et al. 2003; Srinivasan et al. 2009, *Spitzer* Space Telescope; Cutri et al. 2014, Wide-field Infrared Survey Explorer (WISE); Vandenbussche et al. 2002, Infrared Space Observatory (ISO)/Short Wavelength Spectrometer (SWS); Trams et al. 1999, ISO/Infrared Photo-polarimeter (PHT)). We also derived an *HK*-band spectrum from the archival SOFI data taken with a spectral resolution of 1000 (the reduction of the SOFI data is described in Appendix F). The spectrum obtained at 3.95–4.10 μm with ISAAC in 2001 (Matsuura et al. 2005) is flat, without noticeable signatures of the SiO bands[3], consistent with the ISO/SWS data. These (spectro)photometric data show the spectrum of the RSG with H_2O absorption bands, as is indicated in Fig. 3a.

On the other hand, Fig. 3b shows near-infrared spectra of WOH G64 taken more recently with VLT/X-shooter (Program ID: 097.D-0605(A), P.I.: S. Goldman; see Appendix G for details of the X-shooter data) and GRAVITY as well as the REM/REMIR *JHK′* photometric data. Because the absolute flux calibration of the X-shooter and GRAVITY spectra is uncertain, we tentatively scaled them to the REM/REMIR *K′*-band flux just to compare the spectral shape (the absolute flux scale likely varied among the X-shooter, GRAVITY, and REM observations). The X-shooter, GRAVITY, and REM/REMIR data all indicate a monotonically rising continuum. This is in marked contrast to the RSG spectrum seen in Fig. 3a. The H_2O absorption is also much less pronounced in the X-shooter spectrum compared to the SOFI data. The molecular spectral features in cool variable stars like WOH G64 change with the variability phase and cycle. The bars of the *JHK* photometric data in Fig. 3a show the variability amplitudes measured from March 1995 to April 1998 by Whitelock et al. (2003). The variability amplitudes measured from January 1987 to November 1991 by Wood et al. (1992) are similar[4]. The rising continuum spectrum is difficult to explain by the variability seen in the *J*, *H*, and *K* bands.

[3] The absolute flux scale is uncertain by a factor of two, which is why the ISAAC spectrum was not included in Fig. 3

[4] The variabilities in the *J* and *H* bands measured by Wood et al. (1992) are not shown in Fig. 3a, because they overlap with those measured by Whitelock et al. (2003). Only the *K*- and *L*-band variabilities are indicated with the bars.

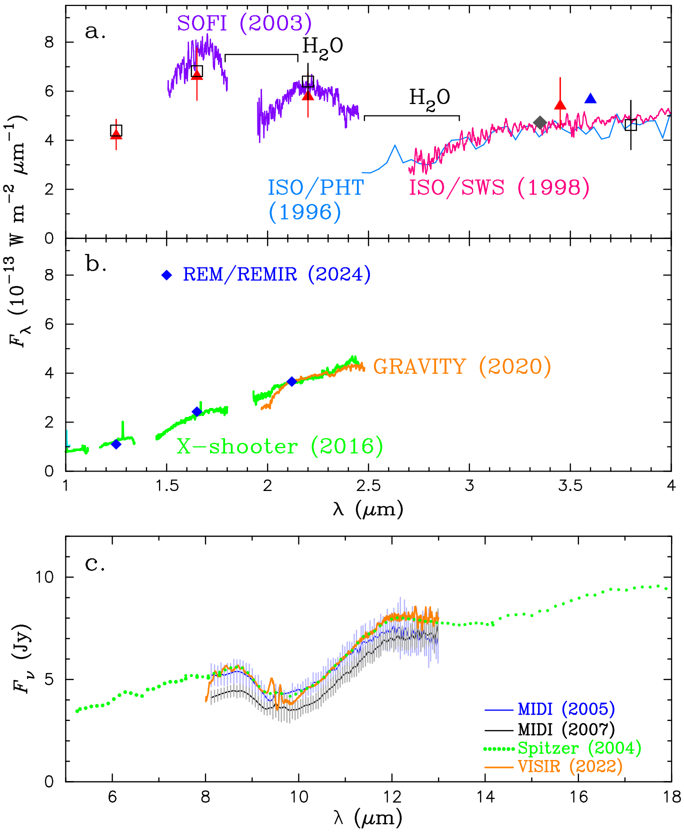

Fig. 3. Near- and mid-infrared spectrum of WOH G64. **a:** Spectrophotometric and photometric data taken at 1–4 μm before 2010. The light blue, pink, and violet lines represent the spectra taken with ISO/PHT in 1996, ISO/SWS in 1998, and SOFI in 2003, respectively. The red triangles and open squares correspond to the photometric data from Whitelock et al. (2003) and Wood et al. (1992), respectively. The bars show the (peak-to-peak) variability amplitudes, not the measurement errors. The gray diamond and blue triangle represent the photometric data taken with WISE in 2009–2010 and *Spitzer* in 2005-2006, respectively. The H_2O absorption features in the RSG spectrum are also indicated. **b:** Spectra of WOH G64 taken more recently. The green and orange lines represent the spectra taken with X-shooter in 2016 and GRAVITY in 2020, respectively. The blue diamonds show the *JHK′* photometric data taken in 2024 with REM/REMIR. The GRAVITY and X-shooter data are scaled to the REM/REMIR *K′*-band flux. The spikes in the X-shooter spectrum as well as the very tiny peak at ~2.16 μm in the GRAVITY spectrum are the residual of the correction for the absorption lines in the spectrum of the calibrator. **c:** Mid-infrared spectra of WOH G64 showing the 10 μm silicate feature in absorption. The blue and black lines represent the spectra obtained with MIDI in 2005 and 2007, respectively, by Ohnaka et al. (2008). The dotted green line shows the *Spitzer*/IRS spectrum taken in 2004, while the orange line corresponds to the VISIR spectrum taken in 2022. The wavelength range between 9.3 and 9.8 μm is severely affected by the telluric absorption.

To examine the spectral variation at longer wavelengths, we obtained a mid-infrared spectrum of WOH G64 at 8–13 μm with VLTI/VISIR at a spectral resolution of 300 (Program ID: 110.23RT.004, P.I.: K. Ohnaka; see Appendix H for details of the observation and data reduction). Figure 3c shows the VISIR spectrum obtained in October 2022 together with the MIDI data taken in 2005 and 2007 as well as the *Spitzer*/InfraRed Spectrograph (IRS) spectrum taken in 2005 and presented in Ohnaka et al. (2008). The VISIR spectrum shows the 10 μm silicate feature in absorption, in agreement with the *Spitzer*/IRS and MIDI spectra within the errors. A comparison of the MIDI and *Spitzer* spectra with other data in the literature presented in Ohnaka et al. (2008, their Fig. 3) indicates that the long-term variation in the mid-infrared spectrum of WOH G64 is small.

5. Discussion and conclusion

The results that the noticeable change in the spectral shape is seen in the near-infrared but not in the mid-infrared may be explained by hot dust forming close to the star. Haubois et al. (2019, 2023) detected dust clouds forming at ~1.5 $R_\star$ around the optically bright RSG Betelgeuse (which is much less dust-enshrouded than WOH G64) by near-infrared and visible polarimetry. They concluded that transparent grains such as Al_2O_3 and Fe-free silicates ($MgSiO_3$ and Mg_2SiO_4) can explain the observed data, although they favor the Fe-free silicates over Al_2O_3. These grains condense close to the star at ~1500 K. Dynamical modeling of winds of asymptotic giant branch stars shows that Fe-rich silicates, whose absorption efficiency is much higher than the aforementioned species, condense onto the transparent grains a little farther out (Höfner et al. 2022). If this also occurs in RSGs like WOH G64, and the grains with mantles of Fe-rich silicates are optically thick in the near-infrared, it could account for the monotonically rising continuum spectrum seen in the near-infrared and the high obscuration of the central star.

The absence of a noticeable change in the mid-infrared spectrum suggests that the hot dust should be confined in a region close to the star. This is in qualitative agreement with the semi-major and semiminor axes of the elongated emission of ~13 and ~9 $R_\star$, respectively. The elongated emission may be due to a bipolar outflow along the axis of the dust torus. Goldman et al. (2017) interpreted the 1612 MHz OH maser emission of WOH G64 at an expansion velocity of 23.8 km s^{-1} as spherical expansion or a bipolar outflow along our line of sight. Alternatively, the elongation may be caused by the interaction with an unseen companion. The torus model of Ohnaka et al. (2008) is characterized by an inner radius of 15 $R_\star$ (2.4 mas), in which the elongated emission with 13 × 9 $R_\star$ (2 × 1.5 mas) can fit, although this cannot be taken as definitive evidence for a companion. Levesque et al. (2009) discussed the possibility of an unseen hot companion and proposed spectroscopy in the blue to prove or disprove the hypothesis. However, neither positive nor negative detections have been reported in the literature.

While the SOFI data taken in 2003 clearly shows the H_2O absorption in the RSG spectrum, the X-shooter spectrum taken in 2016 shows the rising continuum. Therefore, the spectral shape change in the near-infrared should have started at some epoch between 2003 and 2016. Although no near-infrared spectra taken between 2003 and 2016 can be found in the literature, we can set an additional constraint on when the spectral change started as follows. Levesque et al. (2009) derived an extinction toward the central star $A_V = 6.82 \approx \tau_V$ by fitting the visible spectrum of WOH G64 taken in December 2009. This optical depth in the visible translates into $\tau_K = 0.62$ if we adopt the complex refractive index of the warm silicate of Ossenkopf et al. (1992) with the grain size (a) distribution, $\propto a^{-3.5}$, between 0.005 and 0.1 μm, as Ohnaka et al. (2008) assumed (τ_K is lower, 0.18, for a single grain size of 0.1 μm). With $\tau_K < 1$, the central star should still have been visible in the K band in December 2009. Therefore, it is likely that the formation of hot dust started at some epoch between December 2009 and 2016, and had not yet taken place at the time of our MIDI observations in 2005 and 2007.

The formation of new hot dust also means that the central star is now more obscured than the epochs before 2009. We collected

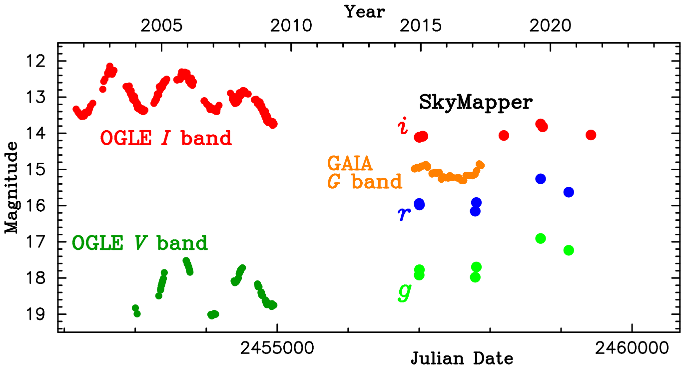

Fig. 4. Visible light curves of WOH G64 from 2001 to 2021. The red and dark green dots represent the photometric measurements in the I and V bands, respectively, from the OGLE project. The orange dots correspond to the *Gaia* data in the G band. The red, blue, and light green dots represent the photometric data from the SkyMapper Southern Survey in the i, r, and g bands, respectively.

visible photometric data from the OGLE project (Soszyński et al. 2009) and SkyMapper Southern Survey (Onken et al. 2024) and show the visible light curves of WOH G64 in Fig. 4. The V- and I-band light curves obtained by the OGLE project show the periodic variation until the middle of 2009. There are noticeable differences in the filter systems between OGLE and SkyMapper. However, the OGLE I band and SkyMapper i band are relatively close, with central wavelengths of 801 nm (OGLE I band) and 779 nm (SkyMapper i band). The SkyMapper i-band data suggest that WOH G64 is fainter after the end of 2014 than in the years covered by the OGLE data. Still, the current sparsity of the data in the literature – particularly between 2010 and 2015, exactly when the formation of hot dust likely started – makes it difficult to examine whether WOH G64 appeared much fainter at the time of our GRAVITY observations in 2020 than in the past.

It is also worth noting that WOH G64 seems to be brighter in the g band than in the V band. Given that the g band is centered at 510 nm, shorter than the OGLE V band at 540 nm, and the visible flux of WOH G64 steeply decreases at shorter wavelengths (van Loon et al. 2005), we do not expect the g-band flux to be higher than the V-band flux. This high g-band flux may be due to the scattering by the transparent grains forming close to the star, as was proposed above, although this is not conclusive. Continuous long-term multiband photometric monitoring covering at least the pulsation period of 840–930 days as well as visible spectroscopic monitoring is necessary to confirm or refute the effects of the new dust formation in the visible.

While the mid-infrared spectrum of WOH G64 shows little long-term change, it is interesting to probe whether there has been a change in the structure of the circumstellar environment on spatial scales larger than the new dust formation region close to the star. The VLTI/MATISSE instrument (Lopez et al. 2022) allows us to obtain spectro-interferometric data in the L (3–4.2 μm), M (4.5–5.0 μm), and N bands (8–13 μm). MATISSE observations and radiative transfer modeling will set much tighter constraints on its circumstellar environment than MIDI did.

Acknowledgements. We thank the ESO Paranal team for supporting our VLTI observations and the d'REM team for carrying out our REMIR observations. K.O. acknowledges the support of the Agencia Nacional de Investigación Científica y Desarrollo (ANID) through the FONDECYT Regular grant 1240301. This research made use of the SIMBAD database, operated at the CDS, Strasbourg, France. This publication makes use of data products from the Wide-field Infrared Survey Explorer, which is a joint project of the University of California, Los Angeles, and the Jet Propulsion Laboratory/California Institute of Technology, funded by the National Aeronautics and Space Administration. This research has made use of the NASA/IPAC Infrared Science Archive, which is funded by the National Aeronautics and Space Administration and operated by the California Institute of Technology. This publication makes use of data products from the Two Micron All Sky Survey, which is a joint project of the University of Massachusetts and the Infrared Processing and Analysis Center/California Institute of Technology, funded by the National Aeronautics and Space Administration and the National Science Foundation. This work has made use of data from the European Space Agency (ESA) mission *Gaia* (https://www.cosmos.esa.int/gaia), processed by the *Gaia* Data Processing and Analysis Consortium (DPAC, https://www.cosmos.esa.int/web/gaia/dpac/consortium). Funding for the DPAC has been provided by national institutions, in particular the institutions participating in the *Gaia* Multilateral Agreement. The national facility capability for SkyMapper has been funded through ARC LIEF grant LE130100104 from the Australian Research Council, awarded to the University of Sydney, the Australian National University, Swinburne University of Technology, the University of Queensland, the University of Western Australia, the University of Melbourne, Curtin University of Technology, Monash University and the Australian Astronomical Observatory. SkyMapper is owned and operated by The Australian National University's Research School of Astronomy and Astrophysics. The survey data were processed and provided by the SkyMapper Team at ANU. The SkyMapper node of the All-Sky Virtual Observatory (ASVO) is hosted at the National Computational Infrastructure (NCI). Development and support of the SkyMapper node of the ASVO has been funded in part by Astronomy Australia Limited (AAL) and the Australian Government through the Commonwealth's Education Investment Fund (EIF) and National Collaborative Research Infrastructure Strategy (NCRIS), particularly the National eResearch Collaboration Tools and Resources (NeCTAR) and the Australian National Data Service Projects (ANDS).

References

Bourges, L., Mella, G., Lafrasse, S., et al. 2017, JMMC Stellar Diameters Catalogue Version 2
Cohen, M., Walker, R. G., Carter, B., et al. 1999, AJ, 117, 1864
Crotts A. P., & Heathcote S. R. 1991, Nat, 350, 683
Cutri, R. M., Wright, E. L., Conrow, T., et al. 2014, AllWISE Data Release (2013)
Ercolino, A., Jin, H., Langer, N., & Dessart, L. 2024, A&A, 685, A58
Gaia Collaboration, Vallenari, A., Brown, A. G. A., et al. 2023, A&A, 674, A1
Goldman, S. R., van Loon, J. Th., Zijlstra, A. A., et al. 2017, MNRAS, 465, 403
Gonneau, A., Lyubenova, M., Lanĉon, A., et al. 2020, A&A, 634, A133
GRAVITY Collaboration, Abuter, R., Accardo, M., et al. 2017, A&A, 602, A94
Haubois, X., Norris, B., Tuthill, P. G., et al. 2019, A&A, 628, A101
Haubois, X., van Holstein, R. G., Milli, J., et al. 2023, A&A, 679, A8
Hofmann, K.-H., Weigelt, G., & Schertl, D. 2014, A&A, 565, A48
Höfner, S., Bladh, S., Aringer, B., & Eriksson, K. 2022, A&A, 657, A109
Humphreys, R. M., Helton, L. A., & Jones, T. 2007, AJ, 133, 2716
Jovanovic, N., Schwab, C., Guyon, O., et al. 2017, A&A, 604, A122
Landri, C., & Pejcha, O. 2024, MNRAS, 531, 3391
Levesque, E. M., Massey, P., Plez, B., Olsen, K. A. G. 2009, AJ, 137, 4744
Lopez, B., Lagarde, S., Petrov, R. G. et al. 2022, A&A, 659, A192
Mason, B. D., Hartkopf, W. I., Gies, D. R., Henry, T. J., & Helsel, J. W. 2009, AJ, 137, 3358
Mathis, J. S., Rumpl, W., & Nordsieck, K. H. 1977, ApJ, 217, 425
Matsuura, M., Zijlstra, A. A., van Loon, J. Th., et al. 2005, A&A, 434, 691
Matsuura, M., Sargent, B., Swinyard, B., et al. 2016, MNRAS, 462, 2995
Molinari, E. 2019, Proceedings: The La Silla Observatory – from the inauguration to the future, https://doi.org/10.5281/zenodo.3245276
Monnier, J. D., Millan-Gabet, R., Tuthill, P. G., et al. 2004, ApJ, 605, 426
Moriya, T. J., Förster, F., Yoon, S.-C., Gräfener, G., Blinnikov, S. I. 2018, MNRAS, 476, 2840
O'Gorman, E., Vlemmings, W., Richards, A. M. S., et al. 2015, A&A, 573, L1
Ohnaka, K., Driebe, T., Hofmann, K.-H., Weigelt, G., & Wittkowski, M. 2008, A&A, 484, 371
Onken, C. A., Wolf, C. Bessell, M. S. et al. 2024, PASA, submitted, DOI:10.25914/5M47-S621
Ossenkopf, V., Henning, Th., Mathis, J. S. 1992, A&A, 261, 567
Pietrzyński, G., Graczyk, D., Gallenne, A., et al. 2013, Nat, 495, 76
Rayner, J. T., Cushing, M. C., & Vacca, W. D. 2009, ApJS, 185, 289
Sana, H., de Mink, S. E., de Koter, A., et al. 2012, Sci, 337, 444
Soszyński, I., Udalski, A., Szymański, M. K., et al. 2009, AcA, 59, 239
Srinivasan, S., Meixner, M., Leitherer, C., et al. 2009, AJ, 137, 4810
Thiébaut, E. 2008, Proc. SPIE. 7013, 70131I
Trams, N. R., van Loon, J. Th., Waters, L. B. F, et al 1999, A&A, 346, 843

Vandenbussche, B., Beintema, D., de Graauw, T., et al. 2002, A&A, 390, 1033
van Loon, J. Th., Zijlstra, A. A., Bujarrabal, V., & Nyman, L.-Å 1996, A&A, 306, L29
van Loon, J. Th., Cioni, M.-R. L., Zijlstra, A. A., & Loup, C. 2005, A&A, 438, 273
Whitelock, P. A., Feast, M. W., van Loon, J. Th., & Zijlstra, A. A., 2003, MNRAS, 342, 86
Wittkowski, M., Langer, N., & Weigelt, G. 1998, A&A, 340, L39
Woillez, J., Abad, J. A., Abuter, R., et al. 2019, A&A, 629, A41
Wood, P. R., Whiteoak, J. H., Hughes, S. M. G., et al. 1992, ApJ, 397, 552
Yaron, O., Perley, D. A., Gal-Yam, A., et al. 2017, Nature Physics, 13, 510
Zhang, J., Lin, H., Wang, X., et al. 2023, Science Bulletin, 68, 2548

Appendix A: Observation log

Table A.1 shows the summary of our GRAVITY observations of WOH G64.

Table A.1. Our VLTI/GRAVITY observations of WOH G64.

#	t_{obs} UTC	B_p (m)	PA (°)	Seeing (″)	τ_0 (ms)	N_{exp}
			WOH G64 DIT = 30 s, N_f = 12			
			2020 December 15 AT configuration: A0-G1-J2-J3			
1	01:57:23	70.9/96.1/123.4/ 56.3/126.1/79.6	−45/−81/59/ 52/26/8	0.57	6.2	1
2	02:42:02	74.3/96.8/121.3/ 55.5/127.7/82.4	−52/−87/50/ 43/16/−2	0.43	6.6	2
3	03:38:15	77.7/96.6/117.7/ 54.1/128.9/85.4	−61/85/39/ 31/3/−15	0.55	6.5	2
4	04:46:15	80.7/94.7/111.4/ 51.6/129.1/88.0	−72/75/25/ 16/−14/−30	0.38	6.6	1
5	05:39:33	81.9/92.0/105.4/ 49.2/128.2/89.2	−81/67/14/ 4/−26/−42	0.31	6.5	1
6	06:30:36	82.4/88.4/98.4/ 46.4/126.7/89.9	−89/60/2/ −8/−38/−53	0.32	7.5	2
7	07:30:54	82.0/83.0/89.8/ 43.0/124.8/90.3	82/51/−11/ −23/−53/−67	0.34	6.9	2
			2020 December 26 AT configuration: A0-B2-C1-D0			
8	01:13:48	18.8/9.4/19.9/ 28.2/32.0/18.6	77/77/8/ 77/42/−20	0.77	3.9	1
9	02:11:48	18.4/9.2/20.8 27.6/31.7/20.0	67/67/−5/ 67/29/−31	0.72	4.3	1
10	04:20:12	16.8/8.4/22.1/ 25.1/30.3/22.1	45/45/−34 45/−1/−56	0.70	4.8	1
11	05:04:03	15.9/7.9/22.3/ 23.8/29.4/22.5	37/37/−43/ 37/−12/−64	0.70	4.7	2

Notes. B_p: Projected baseline length. PA: Position angle of the baseline vector projected onto the sky. DIT: Detector Integration Time. N_f: Number of frames in each exposure. N_{exp}: Number of exposures. The seeing and the coherence time (τ_0) were measured in the visible.

Appendix B: Observed visibilities and closure phases of WOH G64

Figures B.1 and B.2 show examples of the visibilities and closure phases observed at the A0-G1-J2-J3 and A0-B2-C1-D0 configurations, respectively. The observed interferometric data (spectrally binned to the resolution of 330) do not show signatures of the CO bands longward of 2.3 μm.

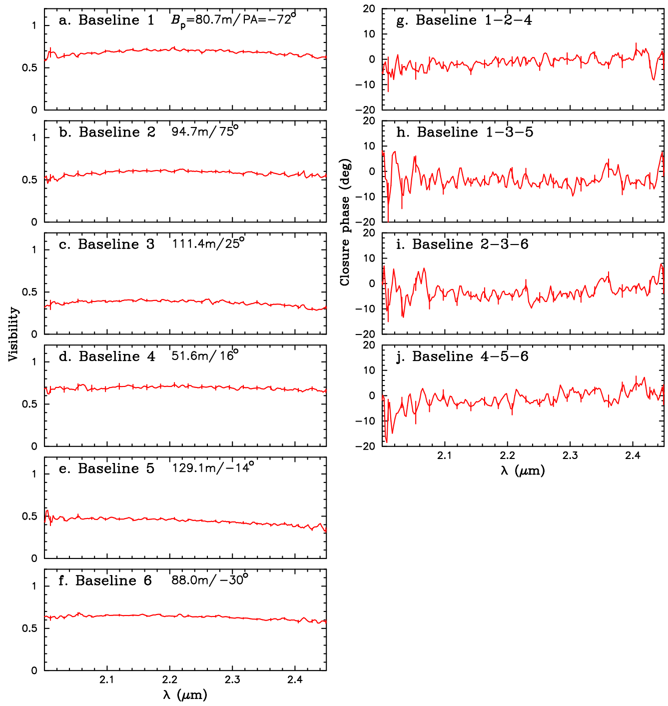

Fig. B.1. Visibilities and closure phases of WOH G64 observed at the A0-G1-J2-J3 configuration. **a–f:** Visibility. The projected baselines (B_p) and position angle (PA) are given in each panel. **g–j:** Closure phase. The baselines that form the telescope triplet are given in each panel.

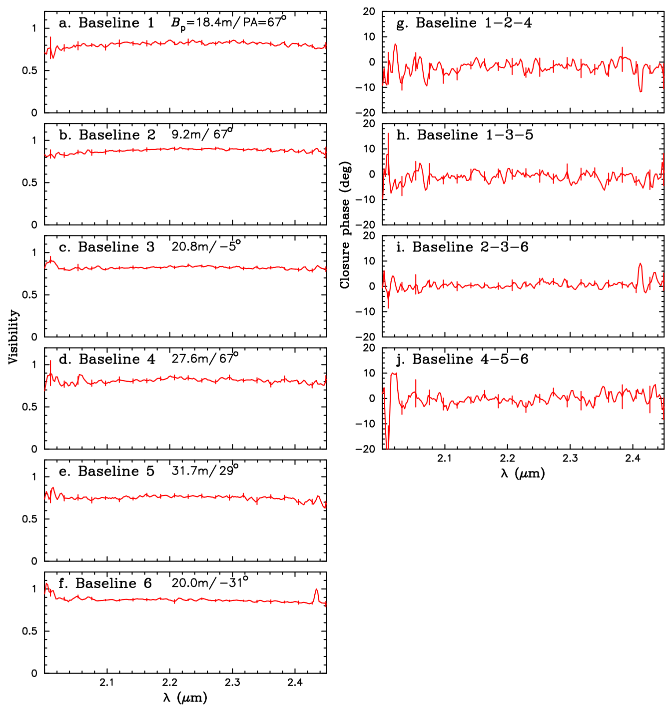

Fig. B.2. Visibilities and closure phases of WOH G64 observed at the A0-B2-C1-D0 configuration, shown in the same manner as Fig. B.1.

Appendix C: Calibration of the GRAVITY spectra

We obtained the spectroscopically calibrated spectrum of WOH G64 as follows:

$$F_{\rm sci}^{\rm true} = \frac{\eta_{\rm cal}}{\eta_{\rm sci}} F_{\rm sci}^{\rm obs} \times \frac{F_{\rm cal}^{\rm true}}{F_{\rm cal}^{\rm obs}},$$

where $F_{\rm sci(cal)}^{\rm true}$ and $F_{\rm sci(cal)}^{\rm obs}$ denote the true and observed spectra of the science target (sci) or the calibrator (cal), respectively. $\eta_{\rm sci(cal)}$ represents the fraction of the flux injected into the fibers of the beam combiner for the science target or calibrator. The spectrum was derived from the data without the spectral binning, because the S/N of the spectral data was sufficiently high. We used the calibrator HD37379 (F6/7V) for the spectrophotometric calibration. To approximate the true spectrum of HD37379, we used the flux-calibrated spectrum of HD126660 (F7V) taken with the InfraRed Telescope Facility (IRTF Spectral Library[5], Rayner et al. 2009) because its spectral type and luminosity class are very close to those of HD37379. The IRTF spectrum taken with a spectral resolution of $\lambda/\Delta\lambda$ = 2000 was convolved to match the spectral resolution of 500 of our GRAVITY (spectral) data and then scaled to match the K magnitude of HD37379 by multiplying by $f_{K,{\rm HD37379}}/f_{K,{\rm HD126660}}$, where $f_{K,{\rm HD37379\,(or\,HD126660)}}$ denotes the K-band flux of HD37379 or HD126660. The spectrum obtained in this manner was used for $F_{\rm cal}^{\rm true}$ in the above spectroscopic calibration.

While the spectra obtained with four ATs agree well in the shape, the absolute flux calibration of the GRAVITY spectra is difficult. First, the fraction of the flux injected into the GRAVITY's beam combiner fibers depends on the performance of the adaptive optics (AO) system NAOMI of the ATs (Woillez et al. 2019). While the calibrator HD37379 is bright enough for NAOMI to work properly, the G-band magnitude of WOH G64 is just at the limit of NAOMI (G = 15), which resulted in degraded AO performance for WOH G64 compared to HD37379. This means that the fraction of the flux injected into the fibers was systematically lower for WOH G64 than for HD37379. Furthermore, the fiber injection fraction also depends on other factors such as the aberration and tip/tilt correction. Jovanovic et al. (2017) show that the coupling efficiency to single-mode fibers varies up to 30%. Given this large uncertainty, we tentatively scaled the GRAVITY spectra to the K'-band magnitude measured with REM/REMIR.

Appendix D: REM observations of WOH G64

The RSG WOH G64 was observed with the REM/REMIR camera with the J, H, and K' filters on 2024 August 11 (UTC). We obtained 10 frames with each filter, using an exposure time of 15 s for each filter. After flat-fielding, sky subtraction, and averaging of the frames, the flux of WOH G64 was measured by PSF (point spread function) photometry and calibrated using five stars in the same field of view, for which the 2MASS JHK_s magnitudes are available. The 2MASS K_s magnitudes were converted to the K' magnitudes using the relations given on the GEMINI web page[6] and the 2MASS web page[7]. The J-, H-, and K'-band fluxes of WOH G64 and their errors are listed in Table. D.1.

[5] http://irtfweb.ifa.hawaii.edu/~spex/IRTF_Spectral_Library/
[6] https://www.gemini.edu/observing/resources/near-ir-resources/photometry/niri-filter-color-transformations
[7] https://irsa.ipac.caltech.edu/data/2MASS/docs/releases/allsky/doc/sec6_4b.html

Table D.1. Near-infrared flux of WOH G64 measured with REM/REMIR on 2024 August 11.

Band	Flux (10^{-13} W m^{-2} μm^{-1})
J	1.10 ± 0.04
H	2.43 ± 0.07
K'	3.66 ± 0.19

Appendix E: Image reconstruction

Comparisons of the visibilities and closure phases computed from the IRBis reconstructed image and the GRAVITY data are shown in Fig. E.1.

The image reconstructed with MiRA using the pixel difference quadratic regularization is shown in Fig. E.2, together with the image obtained with IRBis and the dirty beam. The MiRA image reconstructed with the pixel intensity quadratic regularization is very similar to the one obtained with the pixel difference quadratic regularization. A flat prior was used in both reconstructions with MiRA.

We reconstructed images using the data with spectral windows centered at 2.2 μm with different widths of 0.05, 0.1, and 0.2 μm. The reconstructed images appear to be very similar. Therefore, we show the image obtained with the width of 0.2 μm, which slightly enhances the *uv* coverage.

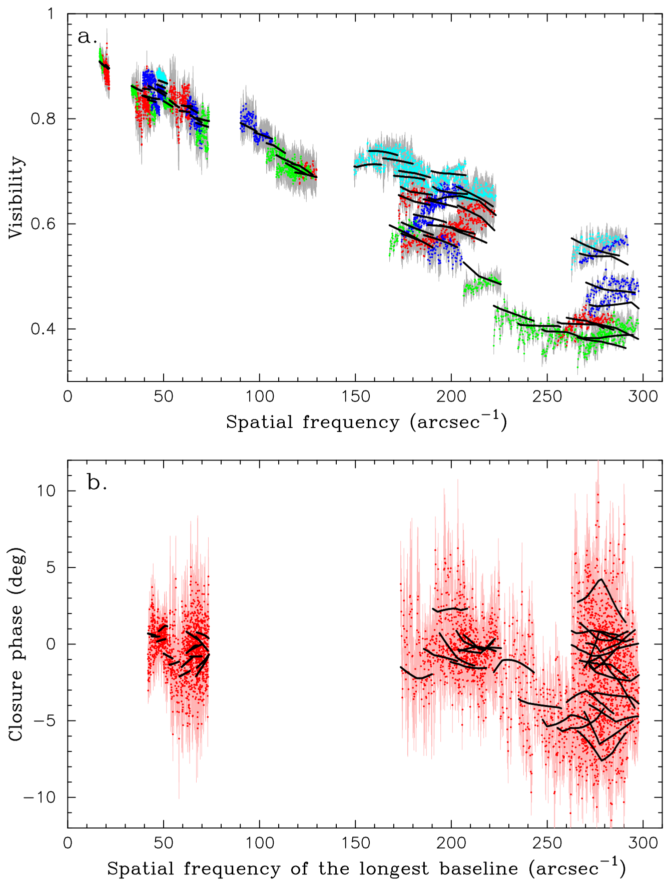

Fig. E.1. Comparison of the visibilities and closure phases of the reconstructed image shown in Fig. 1b with the GRAVITY measurements. **a:** Visibility. **b:** Closure phase. In either panel, the black dots (they appear to be solid lines due to the high density) represent the visibilities or closure phases computed from the reconstructed image. The measurements are shown in the same manner as in Figs. 2b and 2c.

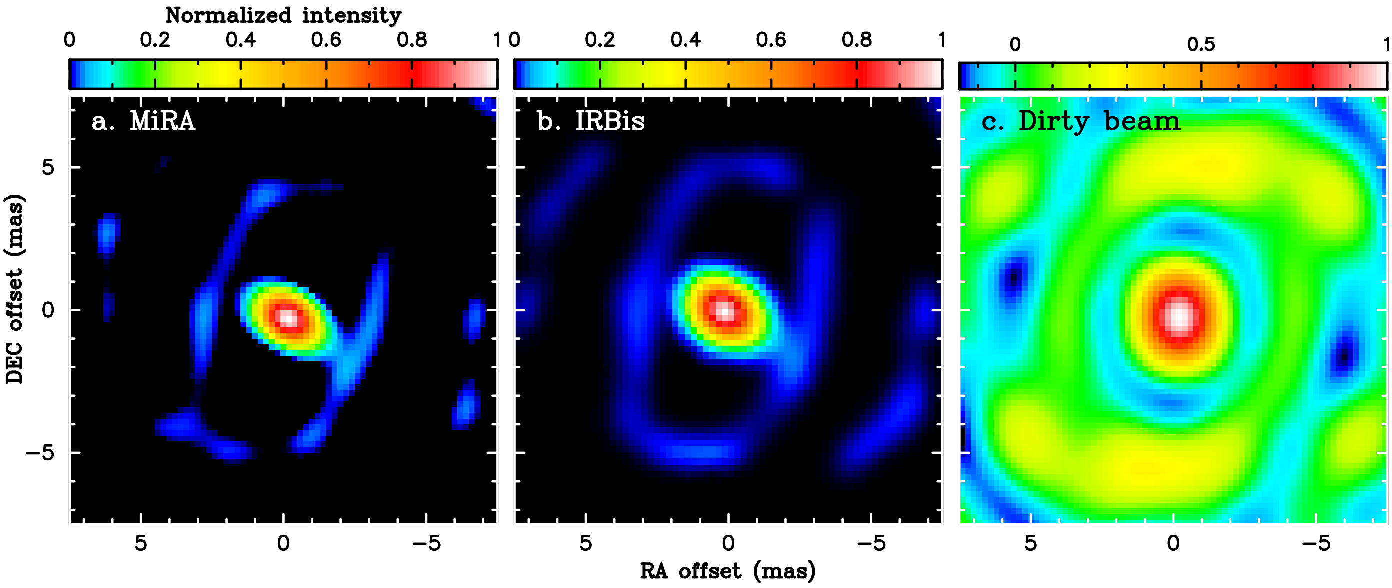

Fig. E.2. Images of WOH G64 reconstructed at 2.2 μm with MiRA and IRBis. **a:** Image reconstructed using MiRA with the pixel difference quadratic regularization. **b:** Image reconstructed with IRBis (the same image as in Fig. 1b). **c:** Dirty beam. North is up, east to the left in all panels.

Appendix F: SOFI observations of WOH G64

We downloaded the SOFI archival data of WOH G64 and the spectroscopic calibrator HIP21984 (G3V) taken on 2003 June 29, covering from 1.5 to 2.5 μm with a spectral resolution of 1000 (Program ID: 71.B-0558(A), P.I.: J. Blommaert). The data were processed with the SOFI pipeline ver. 1.5.12. The spectroscopic calibration of the data of WOH G64 was done in the same manner as described in Appendix C but with both $\eta_{\rm sci}$ and $\eta_{\rm cal}$ set to 1 because they are irrelevant for the SOFI observations. We used HD10697 (G3Va) as a proxy star because of its similarity to HIP21984 with respect to the spectral type and luminosity class. The photometrically calibrated spectrum of HD10697 available in the IRTF Spectral Library (Rayner et al. 2009) was convolved to match the spectral resolution of 1000 of the SOFI data and then multiplied by the K-band flux ratio $f_{K,\,{\rm HIP21984}}/f_{K,\,{\rm HD10697}}$. This was used for $F_{\rm cal}^{\rm true}$ in the spectrophotometric calibration.

Appendix G: X-shooter observations of WOH G64

We downloaded the reduced (phase 3) X-shooter spectra of WOH G64 and the spectroscopic calibrator HIP28322 (B8V) taken on 2016 July 27 (Program ID: 097.D-0605(A), P.I.: S. Goldman). While the reduced data of WOH G64 are spectroscopically calibrated, the telluric lines are not removed. We attempted to remove them as much as possible in the same manner as described in Appendix C with both $\eta_{\rm sci}$ and $\eta_{\rm cal}$ set to 1. To obtain $F_{\rm cal}^{\rm true}$, we used HD147550 (B9V) as a proxy star. Its near-infrared spectrum available in the X-shooter Spectral Library (Gonneau et al. 2020), which is flux-calibrated and telluric-corrected, was scaled to match the K-band flux of HIP28322 and used for $F_{\rm cal}^{\rm true}$ in the spectroscopic calibration. The resulting spectrum was convolved to match the spectral resolution of the GRAVITY spectrum of WOH G64. However, as mentioned in Gonneau et al. (2020), the absolute flux calibration of the X-shooter spectrum is difficult due to the slit loss. Therefore, we tentatively scaled the X-shooter spectrum to match the K'-band flux measured with REM/REMIR.

Appendix H: VISIR observation of WOH G64

Our VISIR observation of WOH G64 at 8–13 μm took place on 2022 October 7 (UTC). A slit width of $1''$ was used, which resulted in a spectral resolution of 300. The data of WOH G64 and the calibrator HD33554 were first reduced with the VISIR pipeline ver. 4.4.2, and the spectrum of WOH G64 was calibrated in the same manner as described in Appendix C with both $\eta_{\rm sci}$ and $\eta_{\rm cal}$ set to 1. We used the absolutely calibrated spectrum of HD33554 presented in Cohen et al. (1999) as $F_{\rm cal}^{\rm true}$.